ELSEVIER

Journal of Nuclear Materials 244 (1997) 1–15

journal of nuclear materials

Macrostructure and microstructure of the carbon fibre composite UAM92-5D-B

V.N. Chernikov [a], W. Kesternich [b], H. Ullmaier [b,*]

[a] *Institute of Physical Chemistry of the Russian Academy of Sciences, Leninsky pr. 31, 117915 Moscow, Russian Federation*
[b] *Institut für Festkörperforschung des Forschungszentrum Jülich, Association EURATOM-KFA, D-52425 Jülich, Germany*

Received 24 June 1996; accepted 30 October 1996

Abstract

A number of methods (TEM, SEM, optical microscopy, EPMA, XRDA) was applied to uncover the architecture and the microstructure of a carbon fibre composite developed in the Russian Federation for application in ITER. The results, especially on microstructure and defects in the different components of this composite enabled the formulation of relations between the microstructural features and the manufacturing procedures which should be representative also for other multidirectional CFCs. Because of their importance for fusion application, special emphasis was devoted (a) to the influence of the different types of inner free surfaces in CFCs on their hydrogen absorption and retention and (b) to the effect of irradiation on microstructural features which govern the mechanical properties, as, for example, toughness.

1. Introduction

The main driving force for the development of carbon fibre reinforced carbon composites (CFCs) was the need to improve the mechanical properties of graphites, particularly, their toughness. While many of the thermal, electrical and chemical properties of CFCs are similar to those of a polycrystalline graphite, their toughness, even at very high temperatures, can be some ten times as high as that of both the carbon fibres and the carbon matrix which form the CFC [1]. The resulting high strength, good thermal conductivity and low thermal expansion of these materials provide their superior thermal shock resistance. This property, the low atomic number and high thermal stability (sublimation point $\approx 3600°C$) make CFCs strong candidates for plasma-facing [2,3] and high heat flux [4,5] components in fusion devices [6,7]. Data on physical and mechanical properties, corrosion and tritium retention for 1D, 2D and 3D CFCs considered as fusion reactor components have recently been reported by Burchell and Oku [8].

The properties of CFCs required for their different applications are tailored by optimum choice of fibre type and content, fibre bundle parameters, matrix precursors and manufacturing routs. Eventually, the properties of a CFC will be determined by both the macrostructure and microstructure of its components and their junctions after completion of the manufacturing process. Therefore, investigations of a CFC structure on different magnification scales are of great importance for both the manufacturers and the users. For the application of CFCs in fusion technology, the parameters of microdefects in the different components are of special interest from the standpoint of hydrogen isotope behaviour.

Most of the structural information on CFCs both before and after different kinds of testing was obtained from observation of specimen (fracture) surfaces in optical or scanning microscopes (SEM) [9,10]. Disadvantages of these methods are poor resolution and relatively weak image contrast for polished surfaces, respectively. The microstructure of individual carbon and graphite fibres has been studied more extensively using a variety of methods [11], including X-ray diffraction (XRD), conventional transmission electron microscopy (TEM) and, more recently, also high resolution TEM (HRTEM) [12,13]. However, these studies were made on isolated fibres in no

* Corresponding author. Fax: +49-2461 616 089.

PII S0022-3115(96)00718-0

relation to their location in CFCs; besides, the fibres had to be viewed by TEM in cross-section after cutting in an ultramicrotome which may have caused artifacts. It thus appeared to be useful to avoid these shortcomings by extending the TEM investigations to the CFC materials in their integrity and, consequently, obtain in situ information not only on the microstructure of the individual CFC components but also on the interfacial regions between them.

In this work we attempted to reach this goal for the material UAM92-5D-B (below designated UAM) which is one of several CFCs offered by the Russian Federation for use in ITER [7,14,15]. Our aims were: (1) determination of UAM architecture and characterization of its main components, (2) detection of chemical heterogeneities, (3) detailed TEM studies of macroscopic and microscopic defects in carbon fibres, fibre bundles, and matrix, (4) evaluation of free inner surfaces appearing between the different structural elements of UAM and finally (5) observation of structure modifications due to radiation damage induced by α-particle implantation at 300 K.

2. Experimental

The main part of the investigations was performed on the 5D-type CFC UAM92-5D-B, manufactured by NPO 'Composit'. According to the supplier's specification, the preform of UAM was formed by hand from fibre bundles of type UKN-5000, consisting of carbon fibres (CFs) produced from polyacrylonitrile (PAN) precursor. The PAN fibres were stabilised at $\cong$ 200°C in air, and the bundles of CFs were carbonized at $\cong$ 2000°C. The composite matrix was created in the course of carbon vapor infiltration (CVI) under a thermal gradient above 1500°C. The product was subjected to a final heat treatment at 2800°C for 2 h in Ar atmosphere.

In order to minimize the hydrogen isotope retention, the material was boronized which was achieved by annealing the composite after saturating it with boric acid, H_3BO_3.

According to our measurements, the density of UAM is 1.87 ± 0.02 g cm^{-3}, which is 17% smaller than the ideal graphite density. A large part of this difference is due to different kinds of porosity. For specimen preparation a block of UAM 24 mm × 24 mm × 10 mm was used.

For comparison, the microstructure of a few other CFCs was also investigated. Among them are: felt CFC Aerolor A05U (Loraine Aerospatial, $\rho = 1.71$ g cm^{-3}); 2D CFC DMS 678 (Dunlop, $\rho = 1.81$ g cm^{-3}); 4D CFC FMI (Fibre Materials Inc., $\rho = 1.82$ g cm^{-3}); felt CFC CX 2002 (Toyo Tanso, $\rho = 1.73$ g cm^{-3}). Detailed data on the architecture and microstructure of these CFCs will be reported elsewhere.

The received block of UAM was cut into smaller pieces by spark erosion or by sawing with diamond blades. Surfaces were ground and polished using SiC based polishing papers with grain sizes down to 0.25 μm under water cooling. Thereafter, specimens were cleaned ultrasonically in acetone, rinsed in methanol and dried at 100°C in air.

Discs of 3 mm in diameter were cut from 300 μm thick plates using an ultrasonic disc cutter in such a way that a particular CFC element of interest (e.g., a fibre bundle in required orientation or matrix) was located in the centre. Then the discs were polished to a thickness of 100–150 μm and dimpled from one side until a thickness of 20–30 μm in the central part was reached. Finally the specimens were thinned from both sides by Ar^+ ions down to electron transparency.

Being in its thickness substantially less than the unit cell of the composite, the final specimens appear to be relatively fragile. In some cases (particularly for DMS 678) a novel technique of sample impregnation with epoxy resin was applied which filled the pores and gave stability to the fragile material.

Plate-like samples of Aerolor A05U, cut out and polished parallel to the pressing axis were homogeneously implanted to a depth of 50–60 μm with α particles having energies within the range from 0 to 11 MeV. The mean helium concentration, c_{He}, was 1750 appm which was accompanied by displacement damage of 0.3 dpa in the implanted layer. Irradiated specimens were ground and dimpled in the same way as above, but only from the one side opposite to the irradiated one.

The microstructure of CFCs is complex and its characterization needs imaging in a range from 10^{-2} to 10^{-9} m. This was achieved by optical microscopy, SEM (including electron probe microanalysis, EPMA) and TEM (including analysis of selected area diffraction patterns, SADP). Furthermore, X-ray diffractometry (XRD) with CoK_α radiation ($\lambda = 0.1789$ nm) was employed.

3. Experimental results and discussion

3.1. Architecture, general features and components of UAM

In Fig. 1 two low magnification optical micrographs of UAM and in Fig. 2 the principal scheme of the bundle architecture (bundle preform) are shown. The micrograph plane in Fig. 1a is close to the *x*–*y* plane, while that in Fig. 1b is close to *x*–*z* or *y*–*z* planes which are equivalent. Fig. 1a implies that cross-sections of bundles in *z*–direction are nearly circular and their mean diameter is 0.80 ± 0.05 mm with maximal diameters up to 1.3 mm.

Bundles lying along *x* and *y* axes and in directions of 45° to them (the latter are hatched in Fig. 2a) differ in thickness. Below, both types of bundles in the *x*–*y* plane are called *x*–*y* bundles. The *x*–*y* bundles are flattened in *z*-direction (see *z*–*x* section in Fig. 1b) resulting in nearly rectangular cross-sections. This is probably due to bundle pressing along *z*-direction during manufacturing. The size

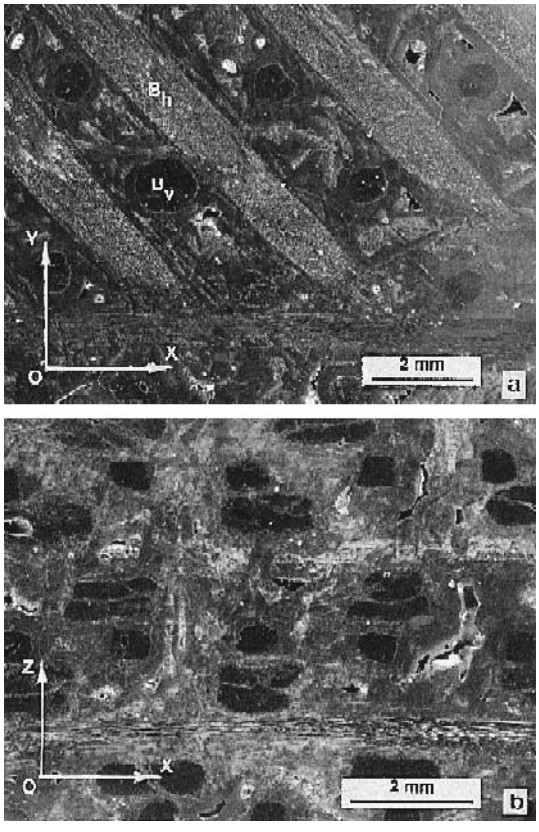

Fig. 1. CFC UAM92-5D-B as seen in a binocular viewer in the direction close to the axes (see Fig. 2): (a) z, (b) y.

of the thin x–y bundles differs from those along z-axis with cross-sections of 0.3 and 0.5 mm^2, respectively. This difference in cross-section is probably due to different constraints during bundle weaving. The unit cell dimension of UAM is 2.8 mm $\times$ 2.8 mm $\times$ 2.8 mm with a bundle volume fraction of 30% (Table 1). The bundle density is estimated to be 10^6 m/m^3.

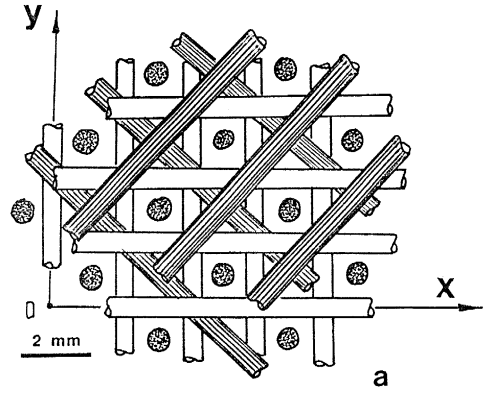

Fig. 2. Principal scheme of the architecture of UAM with a Cartesian coordinate system used in the text.

As evidenced by the micrographs of Fig. 1 many relatively large pores are present in UAM ranging in size from 0.1 to 1.0 mm (with 0.3 mm in average). Most of them are located in the pyrolytic matrix, but some also inside the bundles (Fig. 3a). The majority of these cavities appears to be closed, but some of them are interconnected or linked with cracks along matrix-bundle interfaces (see below) which was manifested by permeability of not too viscous liquids through composite samples of 1 to 2 mm thickness.

Bright contrast in the optical micrographs of Fig. 3a, b and d originates from the pyrolytic matrix. The layered structures show how inter-bundle pockets have been filled in during CVI, and how closed cavities inaccessible for carbon vapor have been formed in the matrix (Fig. 3a). Inner cavity walls are salient and have smooth and brilliant surfaces. According to a rough estimation the presence of these macropores in the matrix accounts for more than 3% of the CFC volume. Fig. 3d shows how individual fibres chipped out off bundles present additional growth centers within inter-bundle pockets providing for their more rapid

Table 1
Some general characteristics of UAM92-5D-B and its elements

	Type/Parameters
Bundles	UKN-5000
Carbon fibres	PAN, ∅7 μm, produced by wet spinning
Carbon fibre structure	turbostratic, transversally isotropic
Unit cell of CFC preform	2.8 mm × 2.8 mm × 2.8 mm
Mean diameter of bundles (in CFC)	0.6–0.8 mm
Specific length of bundles in CFC volume	100 cm/cm^3
Bundle volume fraction	$\leq$ 30%
Fibre density in bundles (in CFC)	(1.0–1.5) × 10^6 cm^{-2}
Volume fraction of fibres in most tightly packed bundles	$\leq$ 65%
Carbon fibre volume fraction in CFC	$\leq$ 20%
Volume fraction of non-graphitizable carbon coats in CFC	6%
Mean c parameter of the matrix and fibres in CFC	(0.3370 ± 0.0005) nm and (0.345 ± 0.005) nm, respectively

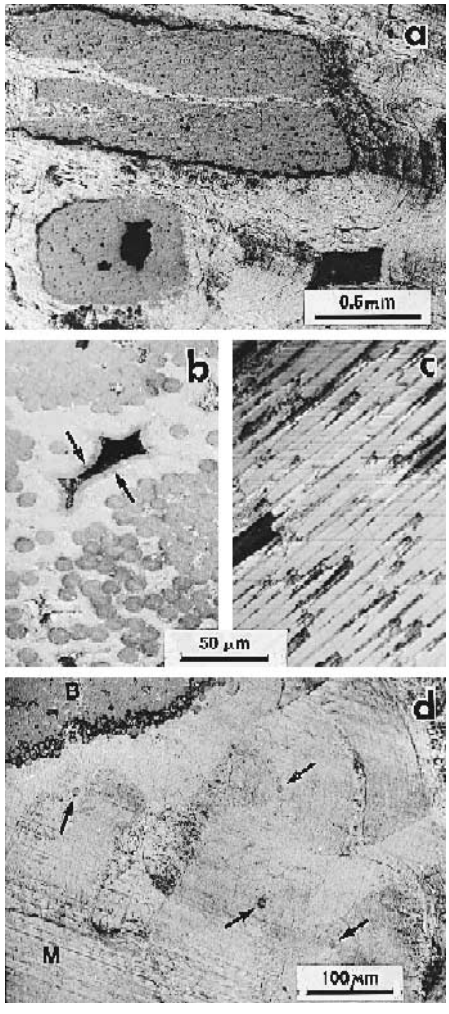

Fig. 3. Optical micrographs of CFC elements at low magnifications: (a) differently oriented fibre bundles — a thick one on top and a thin one at the bottom — surrounded by pyrolytic carbon matrix with macrodefects, (b) transversal cross section of fibres in a bundle (arrows denote a thin crust on the surface of a cavity, see text), (c) cross section of fibres in a bundle oriented at an angle 3–4° to the section plane, (d) occasional individual fibres (denoted by arrows) chipped out off a bundle (B). Deposited layers of pyrolytic carbon (seen as circular traces around such fibres) form the matrix (M) in bundle pockets.

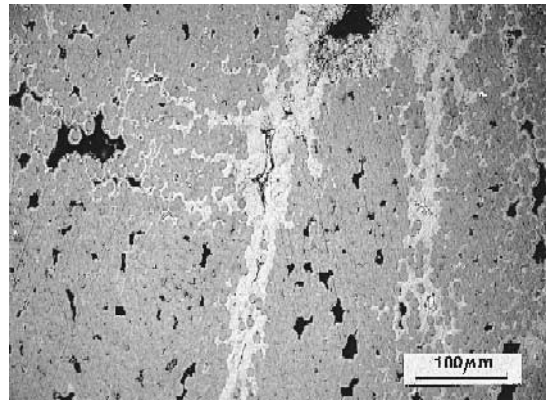

Fig. 4. A part of a bundle with loosely packed carbon fibres (gray) and many needle-like defects (black) which could not be fully healed by pyrolytic carbon (bright) during CVI because of blocking of paths for access of gaseous precursor.

and efficient filling with pyrolytic carbon. Cracks are frequently found along bundle-matrix interfaces (Fig. 3a and d). These cracks have a mean width of 20 μm. The free volume of UAM due to the presence of such cracks is $> 1\%$ (Table 2).

The thickness of pyrolytic carbon layers deposited on bundles and separated fibres varies, reaching a maximum of about 0.5 mm. On the outside of these layers (see dark contrast on the cavity surface in Fig. 3b a 3–5 μm thick crust-like layer exists. Its thickness is constant independent of the thickness of the underlying deposit. Probably, it results from diffusive penetration of non-carbon elements present in the Ar atmosphere at the stage of CFC graphitization at 2800°C.

In Fig. 3b and c areas of bundles in transversal and longitudinal sections are shown. Fibres are about 7 μm in diameter. Within bundles fibres can tightly adjoin to each other, as illustrated in Fig. 3b (upper part) or can be packed loosely (Fig. 3b (lower part) and Fig. 4). The fibre density for tight packing is 1.5×10^{10} m^{-2}. Pyrolytic carbon penetrates into the bundles (light contrast in Fig. 4), and continuous veins are observed between separated parts of thick bundles (see also Fig. 3a, upper bundle). A large number of imperfections within the bundles remains after CVI (Fig. 4, black contrast). Bundle imperfections are

Table 2
Characterisation of porosity in UAM92-5D-B

Type of porosity	Volume fraction, (%)	Inner surface area, S_v (m^2/g)	Characteristic size of a pore
Macroporosity within CFC matrix	> 3	0.00035	300 μm
Macroporosity due to bundle/matrix cracks	> 1	> 0.00025	20 μm
Macroporosity within bundles	> 0.2	> 0.00025	15–20 μm
Interfibre elongated micropores within bundles	≥ 0.05	≥ 0.002	0.5 μm
Fibre/coat microgaps	0.56	$\cong 0.12$	50 nm
Needle-like nanopores within fibres (closed)	$\cong 3.5$	$\cong 30$	$\cong 2.5$ nm
Nanoporosity in isotropic fibre coats	–	6–30	–

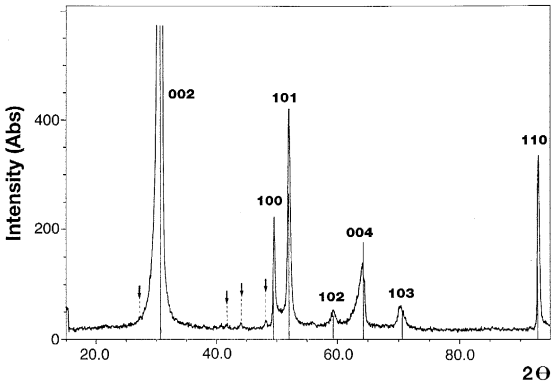

Fig. 5. X-ray diffraction spectra of an UAM section with some glass-like inclusions.

elongated along the bundle axis having needle-like shape with prismatic cross-sections. These macrodefects with mean diameter of 15 to 20 μm and length up to 2 mm are found mainly in *x–y* bundles and account for about 0.6% free volume within bundles and hence for about 0.2% in the CFC as a whole (Table 2).

Each of the UKN–5000 bundles used for assembling the CFC preform consists of 5000 fibres. There are also thick bundles which turned out to be just doubled UKN-5000 bundles.

The volume fraction of fibres in bundles is less than 65% and thus in CFC as a whole less than 20% (Table 1).

Finally it should be mentioned that during sample grinding it turned out that in UAM very hard macroinclu-

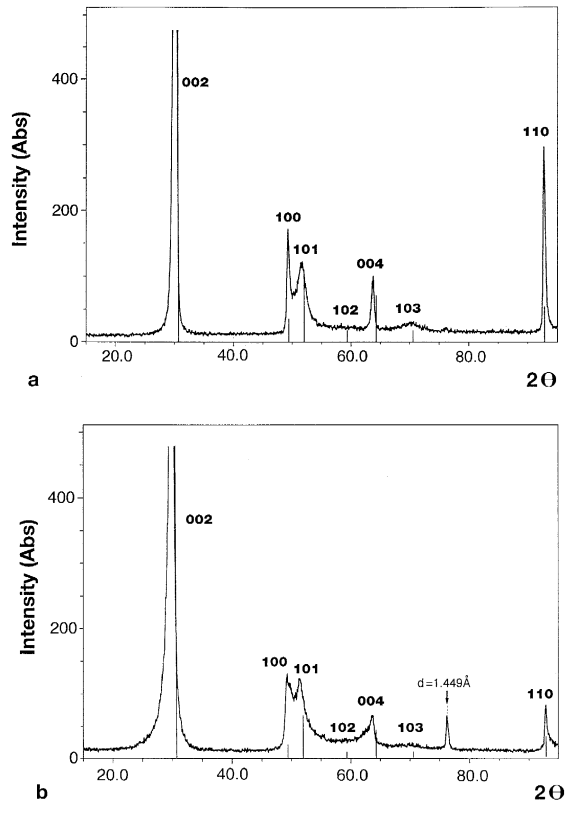

Fig. 6. X-ray diffraction patterns of (a) 4D FMI and (b) felt Aerolor A05U.

Table 3
Interplanar distances for precipitates in pyrolytic carbon of UAM compared with standard diffraction data of B_4C

	Interplanar spacings, *d* (nm), of precipitates based on the analysis (No. of SADPs)						Diffraction characteristics of B_4C [18]	
	9607	9391	9608	9640	9451	9641	*d* (nm)	Intensity
1		0.516						
2		0.437					0.449	30
3							0.402	40
4		0.336			0.338		0.379	70
5	0.279						0.281	30
6	0.256	0.258					0.257	80
7	0.240	0.237	0.239	0.235		0.235	0.238	100
8		0.222					0.230	10
9	0.196	0.201	0.194		0.198	0.192	0.202	10
10						0.178	0.182	10
11			0.168				0.171	30
12		0.166		0.164	0.166		0.164	10
13		0.161				0.163	0.163	10
14			0.149	0.149			0.1505	20
15		0.146					0.1463	30
16							0.1446	30
17		0.135				0.131		
18	0.129	0.129	0.127	0.126	0.127	0.127		

sions with a size of typically 100 μm are present. Apart from carbon, EPMA analysis revealed that the main elements are Si, O and B and possibly C.

3.2. Results of XRD

XRD of UAM was carried out in order to get additional data on the nature of the macroinclusions described at the end of the preceding section and of the mean *c* parameter which is characteristic for the degree of graphitization averaged over the various CFC components.

In Fig. 5 an X-ray diffraction pattern of a UAM section containing one relatively large and some small non-carbon inclusions is presented. All main diffraction maxima belong to graphite. Also some additional very weak reflections (indicated by arrows) were found at angles corresponding to the interplanar spacings, *d*: 0.380, 0.251, 0.2387 and 0.2196 nm. Combining these parameters with the data of EPMA led to the conclusion that the macroinclusions are B_4C (last two columns of Table 3) [18] and/or $B_{12}(C, Si, B)_3$ [17].

The same diffraction pattern (Fig. 5) yields an average *c* parameter of 0.3372 nm for UAM. This value is considerably smaller than the *c* parameter of the fibres (see Section 3.3.4). However, the volume fraction of fibres in UAM is only $\leq 20\%$. This implies a high degree of matrix graphitization at 2800°C.

In Fig. 6 two X-ray diffraction patterns from (a) 4D FMI and (b) felt Aerolor are presented. In both cases the average *c* parameter is higher than for UAM specimens,

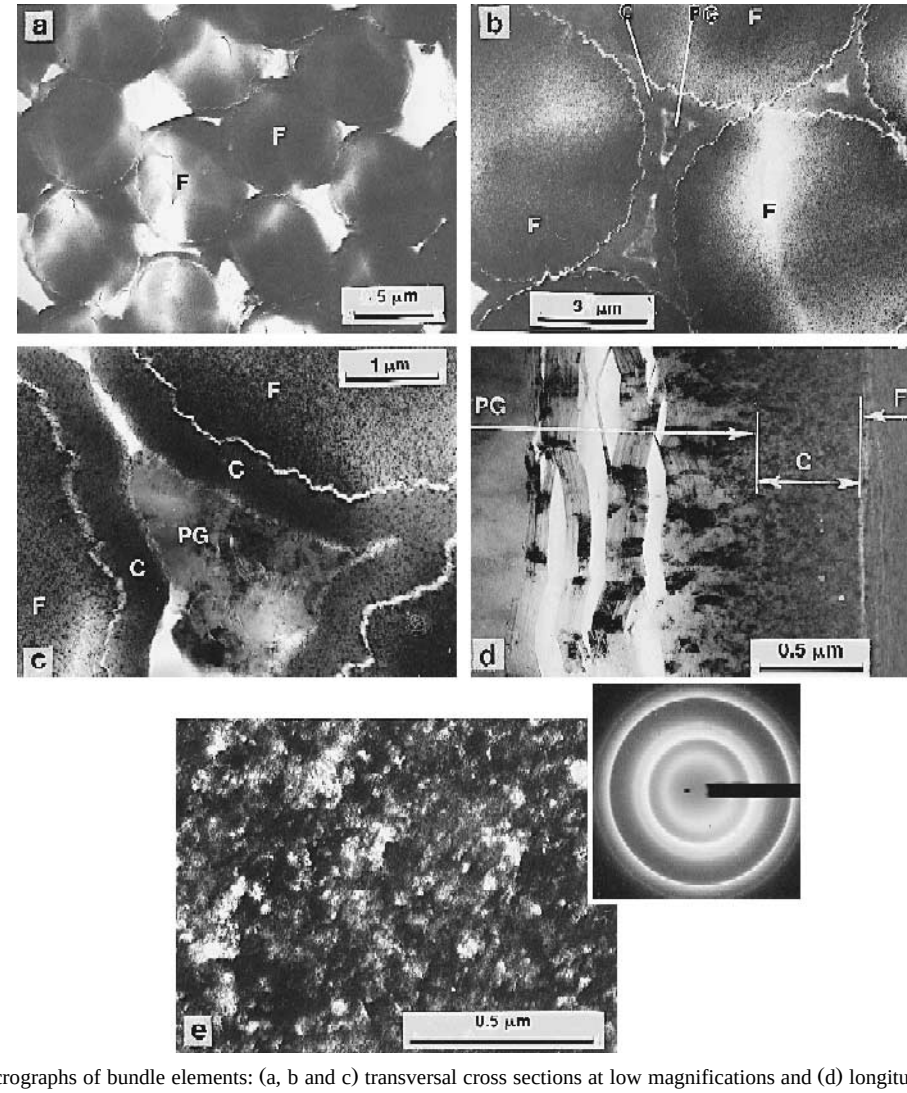

Fig. 7. TEM micrographs of bundle elements: (a, b and c) transversal cross sections at low magnifications and (d) longitudinal cross section at a higher magnification (the multiple crack is a result of delamination within the graphite matrix), (e) dark field of carbon coat imaged in an arc of {002} carbon diffraction ring, with a corresponding SADP in the insert. F: carbon fibre, C: isotropic carbon coat, PG: pyrolytic graphite of the matrix.

namely 0.341 and 0.343 nm, respectively, and also the width of the diffraction maxima is larger than for UAM, especially for the {100} and {101} reflections. All this implies a lower degree of graphitization in these materials compared to UAM. This is not due to a too low temperature of graphitization which is normally not below 2500°C [1], but due to the fact that in FMI the volume fraction of poorly-graphitizing fibres is considerably higher than in UAM, and that in Aerolor a large part of the matrix consists of non-graphitizing isotropic carbon (see below). In the X-ray diffraction pattern of Aerolor a relatively strong maximum was revealed corresponding to $d = 0.1449$ nm. The nature of this reflection is not clear.

3.3. Microstructural investigations by TEM

3.3.1. Fibre bundles

Beyond the magnifications in Figs. 3 and 4 the micrographs in Fig. 7 made at successively increasing magnifications give a clear idea of the bundle structure. The shape of fibre cross-sections is close to circular (Fig. 7a). This indicates that PAN fibres for UKN-5000 bundles are produced by wet spinning into a coagulating bath [1]: diameter and toothed rim shape of the cross-sections of fibres are determined by diameter and micro-indents on inner edges of the spinning jets, respectively (Fig. 7b,c). It is appropriate to note that cross-sections of PAN fibres produced by dry spinning would have a characteristic dogbone or kidney shape.

In agreement with our optical microscope observations (Section 3.1), the packing is far from being close packed. The distances between surfaces of neighbouring fibres (in the absence of macrodefects) vary from 0–4 μm, i.e., neighbouring fibres can touch each other, but can also be apart by a distance comparable to their diameter (Fig. 7a and b). As was established in Section 3.1, a considerable number of elongated macrocracks survives within the bundles. Analysis on specimens of various thickness implies that also microchannels in between neighbouring fibres exist which are not completely filled with pyrolytic deposit (see Fig. 7 a–c). The mean diameter of these microchannels is 0.5 μm, and their volume fraction is about 0.2% with respect to the bundles and 0.05% with respect to the CFC (Table 2).

Fig. 7a–d show that CVI of the bundle preform leads first to the deposition of a thin continuous carbon layer onto the fibre surfaces, coating each individual fibre (denoted by 'C' in Fig. 7). These carbon coats are clearly distinguished from the pyrolytic graphite (denoted by 'PG') subsequently deposited in between fibres.

3.3.2. Carbon fibre coats

The thickness of the fibre coats reaches values between 0.5 and 1.0 μm. Analysis of SADPs and dark field images of the coatings shows that they consist of fine crystalline turbostratic carbon with $d_{002} \cong 0.345$ nm (Fig. 7e). The mean size of crystallites or, using the terminology used in Ref. [1], the mean size $\bar{l}_{LMO}$ of regions of local molecular ordering (LMO) is 10–20 nm. These regions of LMO have to be distinguished from the elementary crystals or basic structural units (BSU) [1] with much lower dimensions characterized by the parameters L_a and L_c. $\bar{l}_{LMO}$ values are uncertain to some extent because LMO regions cannot be uniquely defined, but this is quite usual when describing carbon structures of complicated multilevel hierarchy.

According to our own data, fine-crystalline areas (FCA) are found in many commercial graphites, e.g., EK-98 (Ringsdorf), GB-120 (Toyo Tanso), POCO AXF-5Q (POCO Graphite Inc.), and also in special carbons like PGI (NIIGrafit) [20] produced by carbon vapor deposition

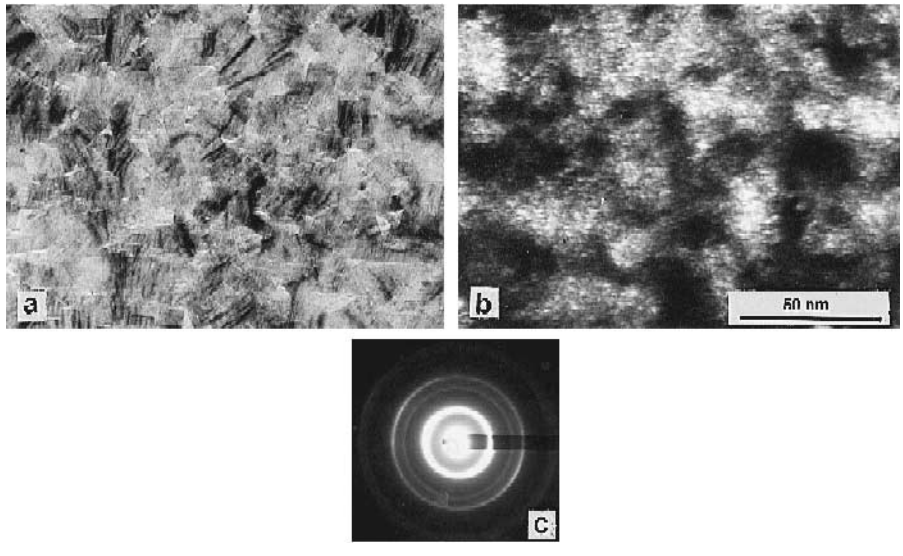

Fig. 8. Carbon fibre in cross section imaged in (a) bright field and (b) dark field in an arc of {002} diffraction ring of SADP (c).

(CVD). The fact that the fine-crystalline structure of the fibre coats does not recrystallize even during final annealing of the CFC at 2800°C means that it is a kind of non-graphitizable isotropic carbon [1]. Taking into account the mean rates of CVD during CVI [1] one can roughly estimate that the time required for such a coat formation is about 10 min. Thereafter, deposition of graphitizable pyrolytic carbon proceeds with a sharp boundary to the fine-crystalline coat. Therefore we have to assume that the CVI conditions change in the course of the infiltration process. Continuing CVI fills the free volume within bundles (see Fig. 7b–d, 'PG') and between them. In general LMO regions, which constitute the fibre coats, vary in size and shape, and even some texture, imposed by the fibres, is possible, due to some variations in local CVD conditions in different regions of the bundles.

Thin FCA coats were revealed also on the surface of fibres in 2D-type DMS-678. Probably, they were also produced unintentionally, in contrast to CFC Aerolor where coatings are the result of a complex densification procedure (see Section 3.4).

3.3.3. Gaps between fibres and coats

When viewing micrographs showing fibre bundles in cross-section (Fig. 7a–c), toothed annular gaps between the fibre surfaces and their coats are clearly recognized. The width of these gaps varies between 35 and 75 nm around a mean value of about 50 nm. In micrographs of longitudinal fibre sections (e.g., Fig. 9), the gaps are practically invisible because their widths are much smaller than the TEM specimen thickness of up to 1 μm or more.

It is almost certain that the gaps are caused by the different shrinkage of coatings and fibres, respectively, during cooling from the CVD temperature of > 1500°C to ambient temperatures. Whereas the coefficient of thermal expansion, α_{th}, is about 17×10^{-6} K^{-1} [11] for PAN fibres in the radial direction (i.e., in preferred $\langle c \rangle$ direction), α_{th} for the fibre coat is below 5×10^{-6} K^{-1} (this value refers to fine-grained graphite MPG-8 [21]). Taking $r_f = 3$ μm as the mean fibre radius and a temperature difference $\Delta T = 1500$ K, these different α_{th} values yield a gap width of about 50 nm in agreement with the observed value. The fact that the gaps appear between the fibres and the coats and not within one of these materials indicates that the bonds within both the fibres and the coats are stronger than the interfacial bonding between them.

Gaps between fibres and their coats (which are not necessarily always fine-crystalline and isotropic) were observed in all CFCs which we have studied. This is understandable since (a) the formation of coats always proceeds at relatively high temperatures even if achieved by other methods than CVD [1] and (b) all fibres are highly textured and have high α_{th} in their radial direction.

These gaps are considered to be an important feature for the high toughness of CFCs [1,22] by providing frictional dissipation of energy along the debonded interface during crack propagation (see also Section 3.4).

3.3.4. PAN carbon fibres

In this section we present TEM data describing the microstructure of the PAN fibres used in UKN-5000 bundles and compare it with structural data on PAN fibres available in the literature. Analysis of micrographs of frequently found fibre cross-sections such as presented in Fig. 8 shows that the shape of regions of local molecular ordering (LMO) is more or less equiaxial in cross-section with a mean size of about 15 nm. Accurate data on the thicknesses L_c of the basic structural units (BSU) in $\langle c \rangle$ directions can be obtained by X-ray methods. TEM data such as in Fig. 8b give only a rough estimate for an upper limit: $L_c \leq 3$ nm. Evaluation of SADPs (Fig. 8c) yields $c = 0.345 \pm 0.005$ nm manifesting a turbostratic structure

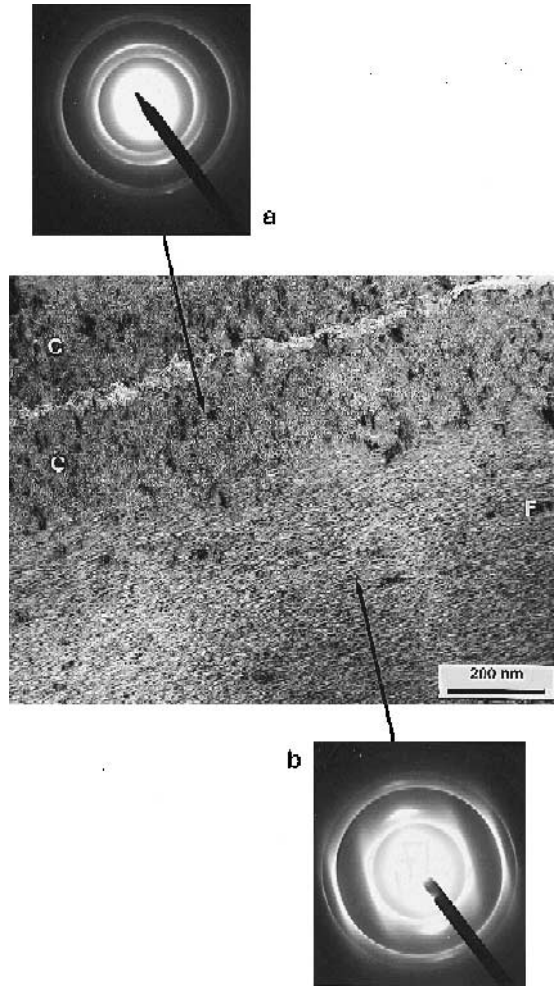

Fig. 9. Longitudinal section of a carbon fibre (F) with its isotropic fine-crystalline coat (C). In inserts are SADPs from: (a) coat and (b) fibre.

which is common for CFC reinforcing carbon fibres. In the particular case presented in Fig. 8c the two weak symmetrical broadenings of the {002} ring are attributed to a slight deviation of the fibre axis from the electron beam, B_e, direction, but not to any ordering of crystallites. When the fibre axis was exactly parallel to B_e, the intensity distribution around the {002} ring was always uniform, and this holds for any selected area (0.5 μm diameter) within the whole cross-section of the fibre (≈ 7 μm diameter). This means that the *c*-axes of LMO regions are distributed isotropically within the fibre cross-section in question. This conclusion is confirmed by image analysis of fibre cross-sections in both bright and dark field. Such a microstructure of fibres is called *transversally isotropic*.

Fig. 9 presents a longitudinal section of a fibre together with its coat and a coat of an adjacent fibre. The SADP in Fig. 9b confirms the preferential orientation of *c*-axes of LMO regions in directions perpendicular to the fibre axis. The SADP from the adjacent coat Fig. 9a corresponds to an almost isotropic structure but clearly shows a small preference of *c*-axes in the same direction as the SADP in Fig. 9b. This is caused by a partly epitaxial growth of the coat imposed by the fibre. A narrow gap between the two coats is visible in contrast to the gap between the fibre and its coat which is invisible due to the reasons explained in the preceding section. In Fig. 10a and b bright and dark field images, respectively, of a longitudinal fibre section are shown. The mean size of LMO regions in the direction of the fibre axis is between 70 and 100 nm with the maximum value of 200 nm as compared to 15 nm for the cross-sectional dimension (the total length of strings of interlinked crystallites, in a manner proposed in Ref. [23], may be higher). The dimension of BSU, L_a, roughly estimated by TEM is about 15–20 nm.

It is worth comparing TEM image contrast of fibres in longitudinal sections and corresponding SADPs with those

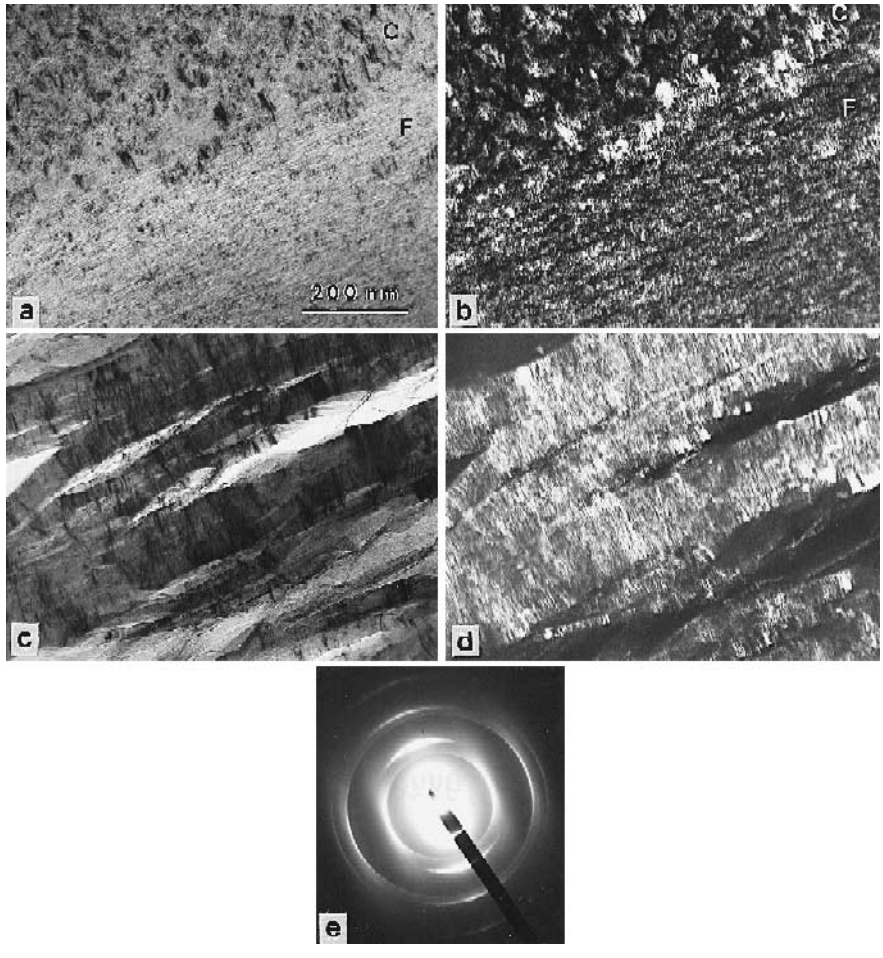

Fig. 10. (a) and (b): Carbon fibre (F) with its coat (C) in comparison with (c and d) pyrolytic graphite (PG) oriented with its basal planes nearly normally to the micrograph plane. Fibre axis coincides with the direction of intersection of PG basal planes by the micrograph plane. (a) and (c) and (b) and (d) are images in bright and dark fields, respectively. (e) SADP from PG (cf. with Fig. 9b).

of edge oriented pyrolytic graphite (EO PG) [24] (see Fig. 10a and b, Fig. 9b, and Fig. 10c–e, respectively). There are two important differences: LMO regions in fibres are much smaller in $\langle c \rangle$ direction and are more strictly parallel to the $\langle a \rangle$ direction than those in PG in the respective directions. Besides, the lamination of PG reveals its relatively poor strength in *c*-direction as compared to the strength of a fibre which is high not only along its axis ($\langle a \rangle$ direction), but also radially ($\langle c \rangle$ direction). The high strength of the PAN fibres is a consequence of an interwoven structure formed by elongated interlinked crystallites [11,16] which provides also for other unique properties, in particular, for their resistance to graphitization.

In the cross-section of UKN-5000 bundles a certain number of fibres exists, the LMO regions of which are not equiaxial and the *c*-axis distribution of which is not random. This is illustrated in Fig. 11. In the three selected areas (A, B and C) LMO regions are reminiscent of thin leaves. While the A area is characterized by a transversally random distribution of crystallites, areas B and C are distinguished by two different predominant orientations of LMO regions. This preferential orientation of LMO regions follows more rigorously from SADP analysis. It is also clearly seen that cavities, presumably elongated (see, for example, [11]) are an inherent feature of such areas. Cavities in area A are lenticular in cross-section (with openings ≤ 10 nm), while the cavities in areas B and C are reminiscent of thin and wide bands with an average thickness of 2–3 nm. The presence of these pores leads to local density variations in the bulk of fibres. As a consequence, ion thinning (when preparing thin sections) proceeds remarkably faster in these areas than in normal areas (with transversally equiaxial LMO regions). The thickness variations are clearly seen in the overall view in Fig. 11a. Such peculiarities of fibres have to be regarded as some kind of defects. In most fibres in UKN-5000 bundles such defects are not pronounced. Thus a transversally isotropic model for the PAN fibres in UAM can be proposed, similar to that suggested in Ref. [12], but, in contrast to the common assumption for PAN fibres, without any sheaths or skins [11].

3.3.5. Implications of CFC defects for the retention of hydrogen

Hydrogen absorption in graphites provided by capillary inflow of H_2 molecules, H atom surface diffusion or bulk diffusion at high temperatures [25] is an important characteristic of these materials as plasma-facing components in fusion devices. Actually, the aim of doping UAM with boron is suppression of hydrogen trapping in both its original and radiation damaged state [20,26].

It is well known that the main reason for hydrogen absorption in graphite is chemisorption of H atoms onto free surfaces of graphite [27,28]. At the same time there is no linear relationship between the concentration of hydrogen occluded by graphite and its specific inner surface area

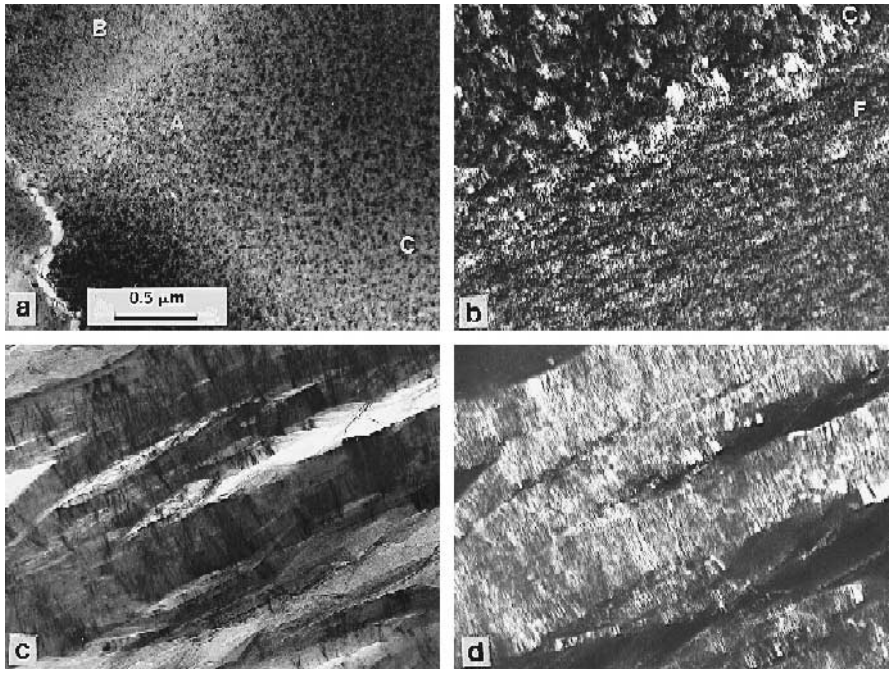

Fig. 11. Peculiarities in the shape and stacking of LMO regions in the cross section of a fibre and an adjacent coat (lower left corner in (a)): (a) general view at low magnification, (b)–(d) show three areas selected in (a), A, B and C, respectively, at higher magnification.

S_v. Two main reasons are responsible for that. First, the adsorption of H atoms occurs on the active surface area (ASA), that is on C atoms terminating basal planes, and, second, the available ASA related to *closed* porosity is scarcely accessible for H atoms. At higher temperatures (≥ 1000°C) penetration of H atoms by diffusion into the bulk of graphite crystals is possible, followed by capture in deep traps [20], but this channel of hydrogen accumulation is beyond the scope of the present paper. Predictions of hydrogen absorption are not reliable due to the complex structure of graphites and especially of CFCs. Therefore we will confine our analysis to an approximate estimation of partial S_v values related to different defects in UAM and to a characterization of potentialities of relevant surfaces with respect to hydrogen adsorption.

The specific inner surface area in a material, S_v, due to any kind of volumetric defects uniformly distributed over its volume is inversely proportional to the characteristic defect size, ξ, and proportional to the volume fraction, $\Delta V/V$, occupied by these defects

$$S_v\,(m^2/g) \cong (k/\xi\rho)\,(\Delta V/V), \qquad (1)$$

where ρ is the density of material and k is the form-factor of the defect. In particular, for spheres $k = 6$ and ξ is the sphere diameter; for infinitely long cylinders $k = 4$ and ξ is the cylinder diameter; for long defects with thin lentil-shaped cross-section $k = 4$ and ξ is the opening height; for long and thin band-like defects $k = 2$ and ξ is the band thickness.

The three types of macropores and the elongated inter-fibre cavities listed in Table 3 have inner surface areas which are much smaller than the BET surface of most nuclear graphites [27] and are also negligible in comparison to the contributions of the various micropores in UAM. A much higher value of $S_v = 0.12$ m^2/g is caused by the fibre/coat gaps and the highest of $S_v = 30$ m^2/g (per 1 g of CFC) by needle-like pores within fibres (Table 2). For the estimation of the latter value the density of fibres was taken to be 1.9×10^6 g m^{-3} which is a typical value for PAN fibres subjected to annealing at temperatures higher than 2500°C [11,16,29], while the mean transversal size of the needle-like pores was estimated on the basis of TEM data to be 2.5 nm, which is in accordance with literature data on parameters of porosity in PAN fibres [11,16,30] [1]. The inner porosity of fibre coats is very high: 100–500 m^2/g referred to the substance itself (isotropic graphite) [1] or 6–30 m^2/g referred to CFC UAM. But, similar to pores in fibres, those in isotropic coats are closed [1,11,16] and, hence, not accessible for any gases.

The value of S_v for fibre/coat gaps (0.12 m^2/g) was evaluated as the inner surface area of two concentric cylinders of corresponding diameters. However, fibres subjected to high-temperature treatment face their surrounding mainly by basal planes [11], that is by non-active planes, while the surface of fine-crystalline isotropic fibre coats is expected to be active for hydrogen adsorption. So, it is more correct to divide the value of S_v for fibre/coat gaps by a factor of two. On the other hand, due to the fact that the inner surface of carbon coats replicating the toothed outer surface of fibres (Fig. 7) is rough, the value of relevant surface area has to be approximately doubled. So the above S_v value can be adopted. This value is close to those found in [31] for 3D CFCs with PAN fibres. So, we come to the conclusion that the specific surface area S_v of CFC UAM will be mainly determined by the inner surface area of carbon coats on fibres and is expected to be about 0.12 m^2/g.

Our conclusion on S_v offers a better understanding of experimental data reported in [28] and cited in [8] according to which CFCs appear to show a somewhat less or at least similar tritium retention as nuclear graphites while pyrolytic graphite demonstrates a much lower tritium retention. To our mind, the latter is not entirely due to the absence of porosity in this material, as it was claimed in [28]. In contrast, the porosity in pyrolytic graphite is relatively high, being $S_v \cong 2.4$ m^2/g according to Eq. (1) applied to data in Ref. [24]. However, the cavities in pyrolytic graphite are closed and are confined by walls non-active for hydrogen adsorption. On the other hand, this fact emphasizes the important role of imperfect intergranular boundaries in nuclear graphites and interfaces in CFCs, respectively, for hydrogen transport and accumulation.

3.3.6. Microprecipitates within bundles

Small perfect crystals and their conglomerates in a size range between 0.1 and 1.0 μm or more were sometimes observed in the pyrolytic graphite deposited between the fibres. A micrograph and a corresponding SADP from such an agglomerate are shown in Fig. 12. Interplanar spacings calculated from a number of SADPs for such crystals together with the reference set of interplanar spacings for B_4C [18] are presented in Table 3. In spite of the limited absolute accuracy of the d_{hkl} determination by means of SADPs ($\geq 2\%$) it is evident that the above mentioned precipitates in UAM are hexagonal boron carbide, B_4C. It is interesting to note that the value $d = 0.516$ nm recorded on one of the SADPs (see Table 3) is close to $d = 0.502$ nm registered during XRD of a pure chemically synthesized B_4C layer [32], while this value is missing among standard d_{hkl} values for B_4C [18]. B_4C inclusions in the same size range were frequently observed even in 'pure' pyrolytic graphites, e.g., of type HPG (Union Car-

[1] It is worth noting that values of S_v due to porosity within fibres based on literature data, reported in Table 8 (p. 109) of Ref. [11], are wrong (about 2–3 orders of magnitude lower than the actual ones) which is, probably, a result of an error in re-calculation of S_v units.

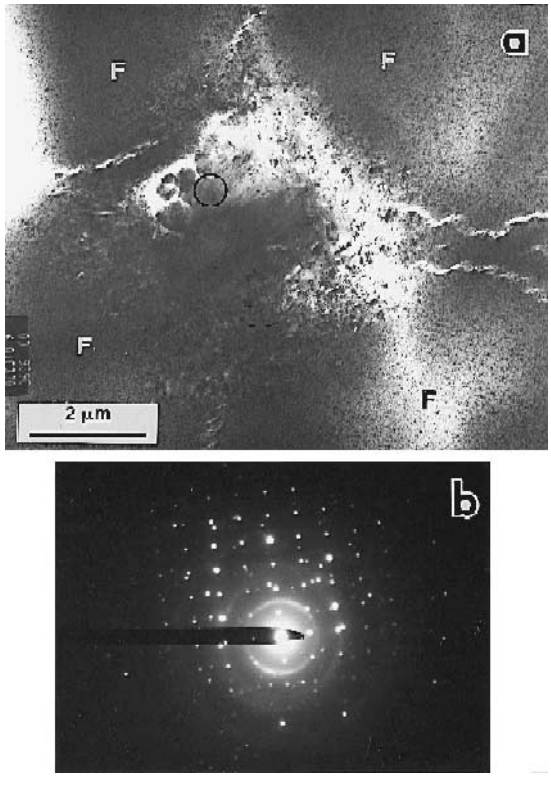

Fig. 12. (a) Conglomerate of B_4C precipitates in the pyrolytic carbon matrix between fibres (F) and its (b) SADP. Selected area in (a) is encircled.

bide). However, the formation of B_4C precipitates in UAM is probably mainly connected with its doping by boron.

3.4. Structure modification of a CFC due to radiation damage

Radiation damage affects key properties of graphites, most strongly at low temperatures [33,34] which is of great importance for their nuclear applications. This degradation is attributed to certain peculiarities of structural changes taking place at irradiation temperatures less than about 300°C [35,36]. It is rather independent of the details of the damage structure, i.e., produced by light ions, neutrons or electrons, but determined by the total damage level [37,38], at least up to 2–3 dpa. Three main effects are registered in graphites within this damage range: radiation-induced swelling (due to c parameter growth [33]), curing of original cracks and strengthening of the graphite matrix [19,24]. It is reasonable to assume that radiation-induced structural modifications proceed similarly in different types of 'pure' graphites or, in other words, most pure graphites damaged at low temperatures are subjected to similar changes on the scale of 'microvolumes'. This is exemplified by the similarity in creation kinetics of deep traps for hydrogen isotopes in different graphites [39,20]. On the other hand, the very different behaviour of these materials under post-irradiation mechanical testing is caused by differences in mutual interaction of their radiation-modified micro-elements and macro-elements. It is therefore clear that a prognosis of mechanical properties of graphites cannot be done solely on the basis of microstructural data received by TEM. Nevertheless, in the frame of this work we have tried to uncover some possible microstructural effects representative for CFCs damaged at room temperature. For this aim Aerolor, a CFC of felt type, was chosen (see Section 2).

Typical micrographs of Aerolor in the original state are presented in Fig. 13a and b. The microstructure of the matrix in this CFC differs considerably from that in UAM. The matrix has a multi-layer structure; it consists of several layers, each having an isotropic structure. The fibres in Aerolor, similar to those in UAM, are covered with coats which are separated from their fibres by gaps with a mean width of 50–70 nm (cf. with Section 3.3.3). In contrast to UAM, these coats are not isotropic, but laminar and graphitizable.

Specimens of Aerolor were damaged to a displacement level of 0.3 dpa by homogeneous α-particle implantation at room temperature up to a helium concentration $c_{He} =$ 1750 appm which is more than one order of magnitude lower than the concentration at which the development of He bubbles in graphites is observed [24]. Analysis of the TEM images (Fig. 13c and d) and SADPs from irradiated specimens reveals features of radiation-induced modifications in all composite elements which are typical also for other graphites irradiated under similar conditions [19,24]. In particular, efficient strengthening and curing of laminated coats take place which are illustrated by comparing Fig. 13a and d. Suppression of diffraction contrast due to a degradation of crystallinity makes it possible to visualize a multilayer structure of the CFC matrix (via mass contrast, Fig. 13c) more distinctly than in the non-irradiated state.

The most important radiation-induced effect consists in a significant narrowing of the gaps between the surfaces of carbon fibres and their coatings (cf. Fig. 13a and d). It is a natural consequence of radiation swelling of CFC elements (particularly pronounced in radial $\langle c \rangle$ directions for highly textured fibres) which obviously also leads to curing of elongated pores on nano-scale present in fibres and of micropores in bundles.

The above effect occurs not only in Aerolor but should be typical for most CFCs, especially for those having fine-crystalline fibre coatings, like UAM. Hence, low-temperature irradiation resulting in tightening of structural elements will lead to an increase of the interfacial (fibre/coat/ . . . /matrix) shear strength and eventually to the reduction of the toughness of CFCs [22]. Such an effect was indeed observed in post-irradiation testing of neutron-irradiated 1D and 2D CFCs [40]. This is in contrast to low dose–high temperature irradiations where shrinkage of

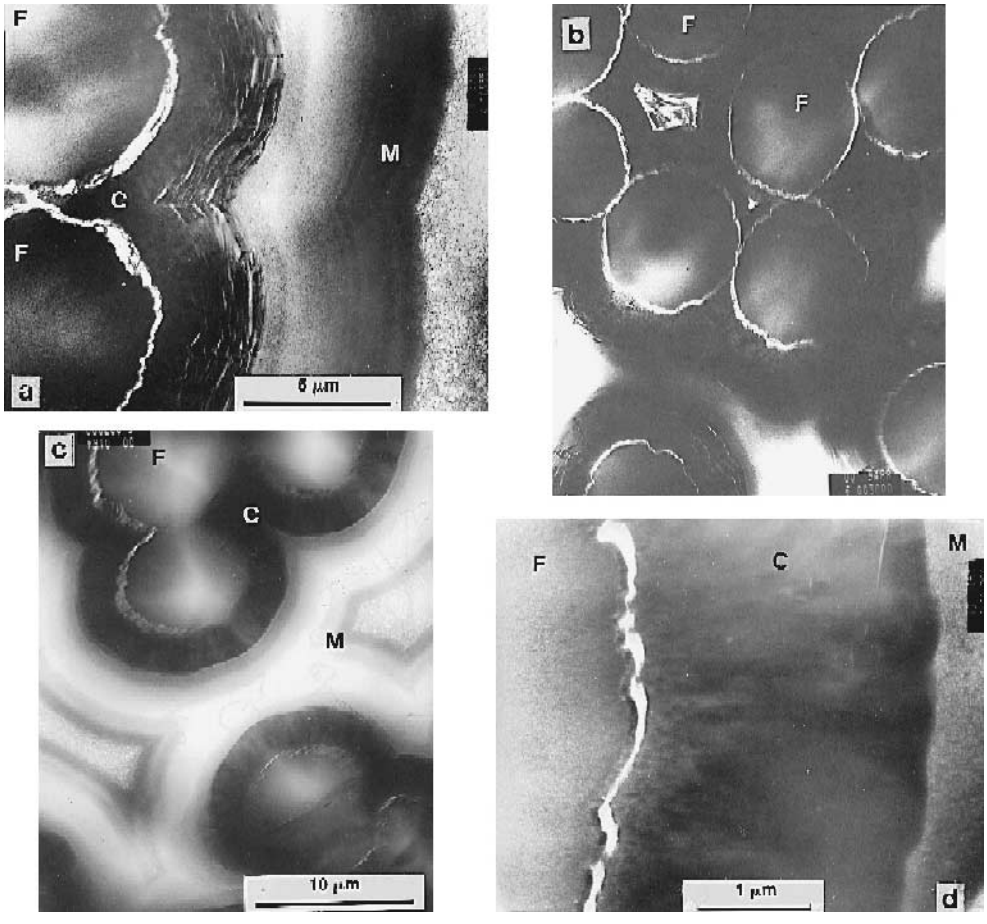

Fig. 13. Felt CFC Aerolor A05U ((a) and (b)) in original state and ((c) and (d)) after displacement damage of 0.3 dpa produced by homogeneous implantation with α-particles up to $c_{He} \cong 1750$ appm ((c) and (d)).

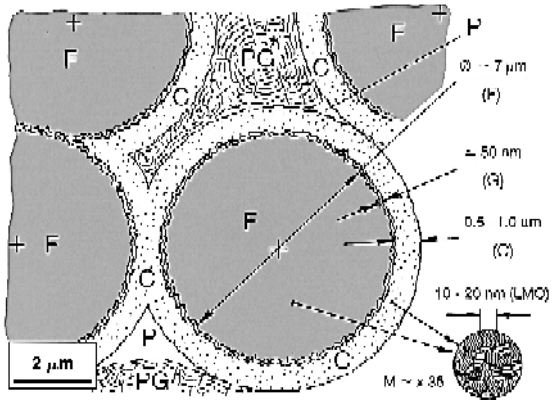

Fig. 14. Schematic presentation of the fibre arrangement in a UKN-5000 bundle in UAM with some characteristic parameters (F: fibre, C: coat, G: fibre/coat gap, PG: pyrolytic graphite produced by CVD, P: interfibre elongated pore within the bundle, LMO: local molecular ordering region). Note many intrafibre microcracks on the enlarged (×35) insert in the lower right hand corner.

CFC components takes place [8] and a slight increase in strength and fracture toughness was observed [41].

4. Summary

(a) A detailed description of the architecture of the carbon fibre composite UAM92-5D-B together with the macrostructure and microstructure of its individual elements is presented. The relations found between the defect structure and the manufacturing procedure seem to be representative also for other multi-directional CFCs. General characteristics of UAM are summarized in Tables 1 and 2, and its typical microstructural features are schematically illustrated in Fig. 14.

It is shown that the PAN fibres in the UKN-5000 bundles have a transversally isotropic structure without any sheath or skin and consist of turbostratic LMO regions. The fibres in bundles are covered by isotropic

non-graphitizing coats formed at the very beginning of the CVD process.

(b) While macroporosity and microporosity account for approximately the same amount of free volume fraction in UAM, microporosity provides the main contribution to the inner free surface area of this material (see Table 2). The main part of this area is attributed to the nano-porosity in the fibres and their isotropic coats, but these pores are closed and thus not decisive for the adsorption of hydrogen isotopes. This holds also for the fibre surfaces consisting mainly of basal, i.e., weakly absorbing planes. We therefore conclude that the inner toothed surfaces of the fibre coats dominate hydrogen adsorption and retention in UAM. Their specific surface area S_v was determined to be about 0.12 m^2/g (referring to CFC UAM).

(c) The fibres have a turbostratic structure with an interplanar spacing of $c \cong 0.345$ nm. The mean value of c for the whole of the CFC $\cong 0.337$ nm which is due to the relatively low volume fraction of fibres (20%) and the high degree of matrix graphitization. Characteristic for the pyrolytic matrix is the observed preferential orientation of basal planes normal to the z-direction of the CFC preform.

(d) At least a part of the alloying boron introduced into UAM for reduction of H-retention is present in the form of microprecipitates of crystalline hexagonal B_4C adjacent to micropores both within the matrix and the bundles. Also, rare but large glass-like particles involving B, O and Si were observed in the matrix and were attributed to occasional precipitates of silicon oxides connected with B_4C and/or the isomorphic compound $B_{12}(C, Si, B)_3$.

(e) A high toughness of a CFC requires a relatively weak bonding between its fibres and the matrix which is provided by definite gaps between their surfaces. Such gaps (with a width of 50 nm in UAM) are formed in all CFCs investigated, obviously, due to the different thermal shrinkage of CFC elements during cooling in the course of the manufacturing process. Radiation-induced swelling of CFC elements (in particular, fibres exhibiting the highest dimensional increase in radial direction) leads to narrowing of these gaps which is connected with the drop of fracture toughness. In this connection low-temperature irradiation ($\leq 300°C$) is most deleterious even for dose levels as low as $\cong 1$ dpa.

(f) The detailed analysis of the UAM92-5D-B microstructure reported in this work together with data reported in Refs. [7,14,15] make it possible to consider this CFC as a promising material for further improvement and eventual application in fusion machines.

Acknowledgements

The authors are grateful to Dr T.A. Burtseva of D.V. Efremov NIIEFA (St. Petersburg, Russia) for supplying the UAM material and some data available on its manufacturing procedure.

References

[1] C.R. Thomas, ed., Essentials of Carbon–Carbon Composites (Royal Society of Chemistry, Cambridge, 1993).
[2] T. Ando, K. Kodama, M. Yamomoto, T. Arai, A. Kaminaga, H. Horiika, M. Eto, K. Fukuda, T. Kiuchi, T. Teruyama, I. Nanai, S. Hanai, S. Ninomiya and M. Tezuka, J. Nucl. Mater. 191–194 (1992) 1423.
[3] R. Matera, G. Federici and the ITER Joint Central Team, in: Fusion Reactor Materials, Abstracts of ICFRM-7. Obninsk, RF, 1995 (SSC of RF, IPP, Obninsk, 1995) p. 8.
[4] P.G. Valentine, R.E. Nygren, R.W. Burns, P. Rocket, A.P. Colleraine, R.J. Lederich and J. Bredley, in: Fusion Reactor Materials. Abstracts of ICFRM-7. Obninsk, RF, 1995 (SSC of RF, IPP, Obninsk, 1995) p. 75.
[5] D.A. Bowers and J.W. Sapp, J. Nucl. Mater. 191–194 (1992) 305.
[6] V.F. Zelensky, V.A. Gurin, Yu.F. Konotop, A.N. Prokopov, S.D. Shirotchenkov, F.P. Belikov, V.A. Kuprijenko, B.V. Samsonov, I.G. Lebedev, N.A. Aksenov, Ya.I. Shtrombakh, V.M. Aleksejev, Yu.G. Bushujev, V.V. Vorobei, V.N. Kirillov, V.A. Sokolov, T.B. Ashrapov and R.G. Khanbekov, in: Radiation Materials Science. Proc. Int. Conf. Rad. Mat. Sci., Alushta, 1990. Vol.3 (KhPhTI, Kharkov, 1990) p. 160 (in Russian).
[7] P.A. Platonov, B.I. Karpukhin, A.A. Mitrophansky, O.K. Chugunov, E.I. Trofimchuk, S.V. Kustchuk, S.I. Aleksejev, V.M. Aleksejev and T.A. Burtseva, in: Radiation Impact on Materials for Thermonuclear Reactors. Proc. 2nd Int. Conf., 1992. Part II (ZNII KM 'Prometheus', St. Petersburg, 1992) p. 409 (in Russian).
[8] T.D. Burchell and T. Oku, in: Atomic and Plasma–Material Interaction Data for Fusion, J. Nucl. Fus. Suppl. 5 (1994) 77.
[9] J.P. Qian, X. Liu and P.Y. Li, J. Nucl. Mater. 191–194 (1992) 340.
[10] M. Akiba, M. Araki, S. Suzuki, H. Ise, K. Nakamura, K. Yokoyame, M. Dairaku and Sh. Tanaka, J. Nucl. Mater. 191–194 (1992) 373.
[11] J.-B. Donnet and R.Ch. Bansal, Carbon Fibres, 2nd Ed. (Marcel Dekker, New York, 1990).
[12] S.C. Bennett and D.J. Johnson, in: Proc. 5th Int. Conf. on Carbons and Graphite. Vol. 1 (Soc. Chem. Ind., London, 1978) p. 377.
[13] H. Shimizu, Sh. Suginuma and Y. Gotoh, J. Nucl. Mater. 176&177 (1990) 1000.
[14] T.A. Burtseva, O.K. Chugunov, E.F. Dovguchits, V.L. Komarov, I.V. Mazul, A.A. Mitrofansky, M.I. Persin, Yu.G. Prokofiev, V.A. Sokolov, E.I. Trofimchuk and L.P. Zav'jalsky, J. Nucl. Mater. 191–194 (1992) 309.
[15] T.A. Burtseva, I.V. Mazul, N.N. Shipkov, V.A. Sokolov, M.I. Persin and O.K. Chugunov, in: Fusion Reactor Materials. Abstracts of ICFRM-7. Obninsk, RF, 25–29, 1995 (SSC of RF, IPP, Obninsk, 1995) p. 176.
[16] A.A. Konkin, in: Heat-, High Heat-Resistant and Noncombustible Fibres, ed. A.A. Konkin (Chimiya, Moscow, 1978) p. 217 (in Russian).
[17] JCPDS-ICDD, 19-178; 42-382; 42-383; 42-392 (1992).
[18] S.S. Gorelik, L.N. Rastorgujev and Yu.A. Skakov, X-ray Diffraction and Electron Diffraction Analysis. Supplement (Metallurgiya, Moscow, 1970) (in Russian).
[19] V.N. Chernikov, A.P. Zakharov, H. Ullmaier and J. Linke, J. Nucl. Mater. 209 (1994) 148.

[20] V.N. Chernikov, A.E. Gorodetsky, S.L. Kanashenko, A.P. Zakharov, W.R. Wampler and B.L. Doyle, J. Nucl. Mater. 217 (1994) 250.
[21] Yu.S. Virgiljev, in: Radiation Impact on Materials for Thermonuclear Reactors. Proc. 2nd Int. Conf., 1992. Part I, p. 35 (in Russian).
[22] A.G. Evans and D.B. Marshall, Acta Metall. 37 (1989) 2567.
[23] D. Crawford and D.J. Johnson, J. Microsc. 94 (1971) 51.
[24] V.N. Chernikov, W. Kesternich and H. Ullmaier, J. Nucl. Mater. 227 (1996) 157.
[25] G. Federici and C.H. Wu, J. Nucl. Mater. 186 (1992) 131.
[26] V.N. Chernikov, V.Kh. Alimov, A.E. Gorodetsky, V.M. Sharapov, A.P. Zakharov and E.I. Kurolenkin, J. Nucl. Mater. 191–194 (1992) 320.
[27] J.P. Redmond and P.L. Walker Jr., J. Phys. Chem. 64 (1960) 1093.
[28] R.A. Causey, J. Nucl. Mater. 162–164 (1989) 151.
[29] D.A. Kuznetsova, E.I. Kurolenkin, Yu.S. Virgiljev, V.I. Kostikov and N.V. Shevenkova, in: Radiation Materials Science. Proc. Int. Conf. Rad. Mat. Sci., Alushta, 1990, Vol. 8 (KhPhTI, Kharkov, 1991) p. 83 (in Russian).
[30] D.J. Johnson and C.N. Tyson, Brit. J. Appl. Phys. 2D (1969) 787.
[31] L.E. Jones, P.A. Thrower and P.L. Walker Jr., Carbon 24 (1986) 51.
[32] V.N. Chernikov, unpublished data.
[33] B.T. Kelly, Physics of Graphite (Applied Science, London, 1981).
[34] V.V. Goncharov, N.S. Burdakov, Yu.S. Virgiljev, V.I. Karpukhin and P.A. Platonov, Radiation Effects in Fission Reactor Graphites (Atomizdat, Moscow, 1978) (in Russian).
[35] B.T. Kelly, J. Vac. Sci. Technol. A4 (1986) 1171.
[36] T. Iwata and H. Suzuki, In: Rad. Damage in React. Mats., Proc. of the Symp. in Venice, 1962 (IAEA, Vienna, 1963) p. 565.
[37] R. Niwase, M. Sugimoto, T. Tanabe and F.E. Fujita, J. Nucl. Mater. 155–157 (1988) 303.
[38] M.S. Dresselhaus and R. Kalish, Ion Implantation in Diamond, Graphite and Related Materials (Springer, Berlin, 1992).
[39] W.R. Wampler, B.L. Doyle, R.A. Causey and K.L. Wilson, J. Nucl. Mater. 176&177 (1990) 983.
[40] E.J. Walker, L.F. Pain and P.B. Roscoe, in: Proc. 2nd Int. Carbon Conf. (Deutsche Keram. Gesellschaft, Baden-Baden, 1976) p. 326.
[41] S. Sato, A. Kuramada, K. Kawamata and R. Ishida, Fusion Eng. Des. 13 (1990) 159.